ISSN 1674-1056
http://cpb.iphy.ac.cn
http://iopscience.iop.org/cpb
中国物理 B
Chinese Physics
中国物理 Chinese Physics B

Raman spectroscopy characterization of two-dimensional materials

Fang Liang(梁芳), Hejun Xu(徐何军), Xing Wu(吴幸), Chaolun Wang(王超伦), Chen Luo(骆晨), Jian Zhang(张健)
Citation: Chin. Phys. B . 2018, 27(3): 037802. **doi:** 10.1088/1674-1056/27/3/037802

Journal homepage: http://cpb.iphy.ac.cn; http://iopscience.iop.org/cpb

What follows is a list of articles you may be interested in

A general method for large-scale fabrication of Cu nanoislands/dragonfly wing SERS flexible substrates

Yuhong Wang(王玉红), Mingli Wang(王明利), Lin Shen(沈琳), Yanying Zhu(朱艳英), Xin Sun(孙鑫), Guochao Shi(史国超), Xiaona Xu(许晓娜), Ruifeng Li(李瑞峰), Wanli Ma(马万里)
Chin. Phys. B . 2018, 27(1): 017801. **doi:** 10.1088/1674-1056/27/1/017801

Raman scattering studies on the collapsed phase of $CaCo_2As_2$

Jianting Ji(籍建葶), Anmin Zhang(张安民), Run Yang(杨润), Yong Tian(田勇), Feng Jin(金峰), Xianggang Qiu(邱祥冈), Qingming Zhang(张清明)
Chin. Phys. B . 2016, 25(6): 067803. **doi:** 10.1088/1674-1056/25/6/067803

High-temperature Raman spectroscopic study of vanadoborate $Na_3VO_2B_6O_{11}$

Ji Zhang(张季), De-Ming Zhang(张德明), Qing-Li Zhang(张庆礼), Shao-Tang Yin(殷绍唐)
Chin. Phys. B . 2016, 25(3): 037802. **doi:** 10.1088/1674-1056/25/3/037802

Synthesis, structure, optical, and electric properties of Ce-doped $CuInTe_2$ compound

Fu Li, Guo Yong-Quan
Chin. Phys. B . 2014, 23(12): 127801. **doi:** 10.1088/1674-1056/23/12/127801

Three-dimensional noble-metal nanostructure：A new kind of substrate for sensitive, uniform, and reproducible surface-enhanced Raman scattering

Tian Cui-Feng, You Hong-Jun, Fang Ji-Xiang
Chin. Phys. B . 2014, 23(8): 087801. **doi:** 10.1088/1674-1056/23/8/087801

TOPICAL REVIEW — Thermal and thermoelectric properties of nano materials

Raman spectroscopy characterization of two-dimensional materials*

Fang Liang(梁芳)†, Hejun Xu(徐何军)†, Xing Wu(吴幸)‡, Chaolun Wang(王超伦), Chen Luo(骆晨), and Jian Zhang(张健)

Shanghai Key Laboratory of Multidimensional Information Processing, Department of Electronic Engineering, East China Normal University, Shanghai 200241, *China*

(Received 16 November 2017; revised manuscript received 22 December 2017; published online 13 February 2018)

Two-dimensional (2D) materials have become a hot study topic in recent years due to their outstanding electronic, optical, and thermal properties. The unique band structures of strong in-plane chemical bonds and weak out-of-plane van der Waals (vdW) interactions make 2D materials promising for nanodevices and various other applications. Raman spectroscopy is a powerful and non-destructive characterization tool to study the properties of 2D materials. In this work, we review the research on the characterization of 2D materials with Raman spectroscopy. In addition, we discuss the application of the Raman spectroscopy technique to semiconductors, superconductivity, photoelectricity, and thermoelectricity.

Keywords: Raman, MoS_2, graphene, 2D materials, non-destructive characterization

PACS: 78.66.–w, 78.20.–e **DOI:** 10.1088/1674-1056/27/3/037802

1. Introduction

Graphene has become a hot research topic in recent years because of its outstanding optical, electronic, and other physical properties, such as large specific surface area, ultrahigh carrier mobility, excellent thermal conductivity, and optical transparency.[1–9] However, graphene lacks the electronic bandgap, which limits its applications in electronic transistors. Therefore, researchers are exploring other two-dimensional (2D) materials with bandgaps, such as transition metal dichalcogenides (TMDs) and black phosphorus (BP).[10–17] Various 2D materials beyond graphene have been explored,[8,18] including insulators (h-BN,[19] HfS_2[20]), topological insulators (Bi_2Se_3,[21] Sb_2Te_3[22]), semiconductors (MoS_2,[23] $MoSe_2$,[24] TaS_2,[25] $MoTe_2$,[26] WSe_2[27]), semimetals ($NiTe_2$,[28] VSe_2[29]), and superconductors ($TaSe_2$,[30] $NbSe_2$[31]). These materials combine the strong covalent in-plane bonding with weak van der Waals (vdW) out-of-plane interactions.[32,33] 2D materials exhibit remarkable thermoelectric, conductive, superconductive, optical, and photovoltaic characteristics and hold potential for applications in nanoelectronics and optoelectronics devices.[34–48]

The characterization of materials is important to identify and explore their structure. Raman spectroscopy is a powerful and non-destructive characterization tool to study 2D materials. It has the capability of characterizing the structural properties of 2D materials, as well as detecting the layer thickness, band structures, strain effects, doping type, concentration, electron–phonon coupling, and interlayer coupling.[49–52] This review mainly focuses on Raman spectroscopy applied to studying 2D materials. Figure 1 shows an overview of Raman characterization efforts for 2D materials and their applications.

This review is arranged as follows: firstly, the basic theory of Raman spectroscopy is introduced. Secondly, we discuss the symmetry and thickness of 2D materials, as well as the effects of strain, substrate, and laser power on 2D materials detected by Raman spectroscopy. Then, various applications of Raman spectroscopy involving 2D materials are reviewed. Finally, a summary and outlook are provided for the development of Raman spectroscopy of 2D materials in the future.

2. Raman spectroscopy

In 1928, Indian experimental physicist Raman discovered a light-scattering effect. The optical frequency changes when light is scattered by a medium due to the interaction between the incident light and molecular motion. The scattered radiation with energy lower than the incident radiation is named the Stokes line, while that with energy higher than the incident radiation is named the anti-Stokes line. The wavenumbers of the Stokes and anti-Stokes lines are the direct measurements of the vibrational energies of the molecule. The energy which increases or decreases under the excitation is related to the vibrational energy spacing in the ground electronic state of the molecule. Since the majority of molecules are in the low vibrational energy level due to the Boltzmann distribution at thermal equilibrium, the intensity of the anti-Stokes

*Project supported by the National Natural Science Foundation of China (Grant Nos. 11504111, 61574060, and 61574056), the Projects of Science and Technology Commission of Shanghai Municipality of China (Grant Nos. 15JC1401800 and 14DZ2260800), the Program for Professor of Special Appointment (Eastern Scholar), Shanghai Rising-Star Program, China (Grant No. 17QA1401400), and the Fundamental Research Funds for the Central Universities of China.

†These authors contributed equally to this work.

‡Corresponding author. E-mail: xwu@ee.ecnu.edu.cn

© 2018 Chinese Physical Society and IOP Publishing Ltd

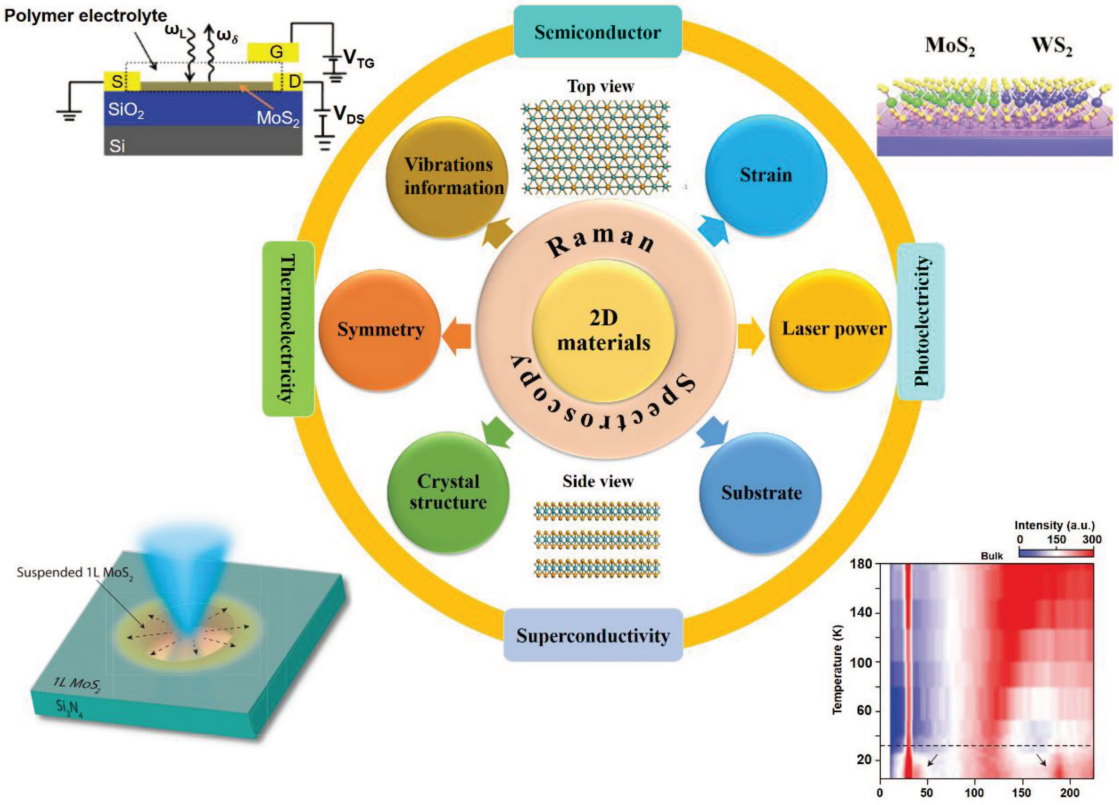


Fig. 1. (color online) Overview of Raman characterization of 2D materials and applications. In this figure, the top left inset is presented with permission from Ref. [113]. Copyright 2012, American Physical Society. The top right inset is presented with permission from Ref. [126]. Copyright 2015, Wiley-VCH Verlag GmbH & Co. KGaA. The bottom left inset is presented with permission from Ref. [64]. Copyright 2014, American Chemical Society. The bottom right inset is presented with permission from Ref. [31]. Copyright 2015, Nature Publishing Group.

transition is weaker than that of the Stokes transition. Raman spectra provide rich information of materials. The full width at half maximum (FWHM) of Raman spectra is an indicator for crystalline quality. Low-frequency Raman modes could provide information such as the layer number, uniformity, crystal structure, and grain boundaries of TMDs.[53]

2.1. Symmetry analysis

TMDs with tunable bandgaps have been widely studied in recent years. From the crystal structure point of view, there are three polytypes of TMDs: 1T, 2H, and 3R. The first Arabic number corresponds to the layer number in the unit cell of each polytype. The letters T, H, and R represent tetragonal, hexagonal, and rhombohedral symmetries, respectively. Each layer contains three atomic planes, where the metal atomic plane is sandwiched between two chalcogen atomic planes like *X*–*M*–*X* (*X* stands for chalcogens and *M* represents transition metals), while different layers are bound by the vdW force. In each layer, for the trigonal prismatic coordination, the positions of the upper and the bottom triangle planes are the same. For the octahedral coordination, the bottom triangle plane is rotated 180° relative to the upper plane. The metal atoms of both the 2H and 3R polytypes are in the trigonal prismatic coordination. The unit cell of the 2H polytype has two *X*–*M*–*X* planes, in which the metal atom of the first *X*–*M*–*X* plane overlaps with the chalcogen of the second *X*–*M*–*X* plane. The unit cell of the 3R polytype consists of three *X*–*M*–*X* planes, in which the second and the third *X*–*M*–*X* planes are obtained by translating the first *X*–*M*–*X* plane by a certain distance along the same direction. The metal atoms of the 1T polytype are in the octahedral coordination. The structure of the 1T polytype has a stacking of *X*–*M*–*X* formed tautologically along the *c*-axis at the position of the following planes, which is the same as the first *X*–*M*–*X* plane. The transition metal atom (or chalcogen atom) overlaps with another transition metal atom (or chalcogen atom). *X* atoms in the upper layer and lower layer are rotated by 60°. The different electronic structures in the monolayer MX_2 depend on the different coordination of metal atoms. For example, monolayer 2H-MoS_2 is semiconducting, whereas single-layer 1T-MoS_2 is metallic. The stacking order is also an important parameter for the symmetry of 2D materials. The 2H polytype has the stacking order of AbA BaB (the capital letters denote chalcogens, and the lower-case letters stand for metal atoms). For the bulk phase of these materials, the symmetry space group is D_{6h}.[54] For few-layer structures, the symmetry space group for odd-number-of-layers 2D materials of the 2H polytype is D^1_{3h} with the hori-

zontal reflection plane (without inversion symmetry).[55] Crystals with an even number of layers belong to the D^3_{3d} group with inversion symmetry.[55,56] The typical stacking order of the 3R polytype is AbA BcB CaC. The stacking of bulk TMDs of the 1T polytype is AbC AbC. The symmetry space group for TMDs of the 1T polytype belongs to D^3_{3d}.

The lattice vibrations of crystals are related to the irreducible representation of the symmetry group. In the following, 2D materials beyond graphene such as MX_2 (M = W, Mo; X = S, Se, Te) are mainly discussed.[47,57–59] Figure 2 shows the representative symmetry and normal mode displacement of several Raman active modes of the 1T, 2R, and 3R polytypes of MX_2. The unit cell of bulk MX_2 consists of six atoms, and there are 18 phonon modes with 3 acoustic modes and 15 optical modes according to the irreducible representation. The lattice vibrational modes of bulk MX_2 at the center of the Brillouin zone can be expressed as:[55,60–63] $\Gamma_{\rm bulk} = A_{1g} + 2A_{2u} + 2B_{2g} + B_{1u} + E_{1g} + 2E_{1u} + 2E_{2g} + E_{2u}$, where one A_{2u} and E_{1u} are transitional acoustic modes, and the other A_{2u} and E_{1u} are infrared (IR) active. A_{1g}, E_{1g}, and E_{2g} are Raman (R) active modes, and B_{2g}, B_{1u}, and E_{2u} are optically inactive (silent) modes. Here, A_{1g} corresponds to the out-of-plane relative motion of X atoms; E_{1g} corresponds to the in-plane relative vibration of X atoms. E_{2g} corresponds to the in-plane opposing motion of M and X atoms. B_{2g} corresponds to the out-of-plane vibration of M and X atomic planes relative to each other. These four modes are the origin of bilayer MX_2 Raman modes.[26] One doubly degenerate E_{2g} mode denoted E^2_{2g} and one B_{2g} mode denoted B^2_{2g} are shear and layer breathing modes in the bulk MX_2, respectively (shear mode and layer breathing mode are discussed in details later in this review). For monolayer MX_2, the unit cell is composed of three atoms with nine normal vibrational modes (6 phonon and 3 acoustic branches) at the Γ point. For multiple-layer MX_2, NL-MX_2 (N stands for the number of layers) there are 9N−3 optical modes, which include 3N-1 vibrations along the c-axis and 3N-1 2-fold degenerate in-plane modes.[18] The irreducible representations of MX_2 with odd and even number of layers at the Γ point can be written as[55,56,62]

$$\Gamma_{\rm odd} = \frac{(3N-1)}{2}(A_2'' + A_1' + E' + E'') + A_2'' + E', \quad N = 1,3,5\ldots,$$

$$\Gamma_{\rm even} = \frac{3N}{2}(A_{1g} + A_{2u} + E_g + E_u), \quad N = 2,4,6\ldots,$$

where E'', A_1', A_{1g}, and E_g are R modes, A_2'', A_{2u}, and E_u are IR modes, and E' is both R and IR active. These Raman modes are not a unique feature of TMDs, but are generally expected in all layered systems with an inversion symmetry center or a horizontal mirror plane. Active Raman modes in few-layer systems are Raman inactive in specific scattering geometries. For example, E_{1g} is inactive in the back-scattering Raman configuration.[30]

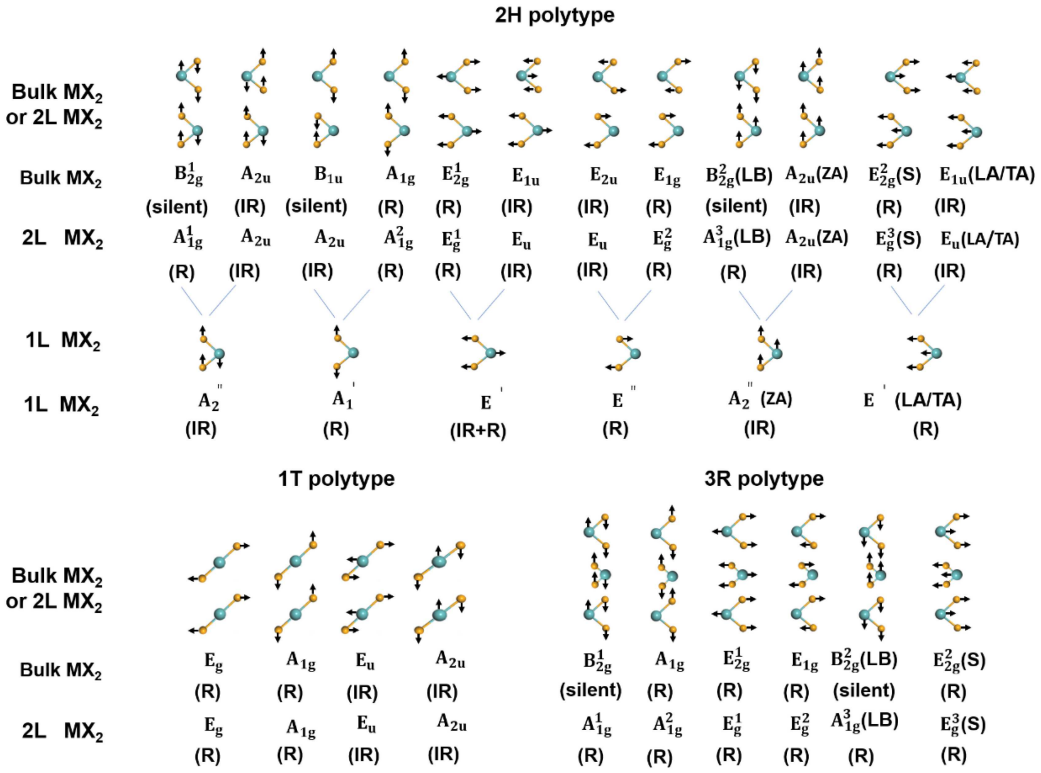


Fig. 2. (color online) Symmetry and normal displacements of optical vibration modes for the 2H-, 3R-, and 1T polytypes of monolayer, bilayer, and bulk MX_2.

2.2. Effect of laser power

In Raman studies, the laser power can be tuned. This provides a useful tool to study the properties of 2D materials related to temperature changes. Generally speaking, the Raman peaks of a suspended MoS_2 flake redshift with the increasing incident laser power (laser power < 1 mW). This phenomenon is due to the thermal expansion of the sample lattice with local heating. Moreover, the thermal expansion of the sample lattice in the out-of-plane direction is more sensitive than in the in-plane direction. Yan *et al.*[64] found that both the A_{1g} and E^1_{2g} peaks of suspended monolayer MoS_2 redshift with the laser power increasing from 0.04 to 0.164 mW (Fig. 3(a)). Meanwhile, they showed that the parameters of the two modes vary slowly and not in a linear way when the laser power is larger than 0.25 mW in their experiment due to the nonlinearity of absorption or the higher orders of temperature-dependent coefficients. However, Miller *et al.*[65] found that the A_{1g} peak redshifts and broadens, whereas the frequency of the E^1_{2g} mode changes negligibly as the laser power increases from 25 to 1000 μW under 488 nm laser excitation for MoS_2 in an ambient environment. Najmaei *et al.*[66] also found that both the A_{1g} and E^1_{2g} peaks of supported 1L MoS_2 redshift with the increasing laser power, and the change for E^1_{2g} is small. The redshifts of the Raman modes with increasing laser power was also found in other 2D materials such as WS_2 and BP. Peimyoo *et al.*[67] found that the A_{1g} Raman modes of mono- and bilayer WS_2 redshift, and their peak intensities are increased with increasing power of a 532 nm laser (Fig. 3(b)). Luo *et al.*[68] found that the Raman modes of BP redshift as the temperature increases. As seen from Fig. 3(c), the A^2_g mode is more sensitive to the temperature. Different edge structures such as zigzag and armchair provide different Raman signal responses. The zigzag-polarized excitation temperature coefficient is larger than that for armchair-polarized excitation, as seen in Fig. 3(d). It may result in anisotropic thermal expansion during the heating process.

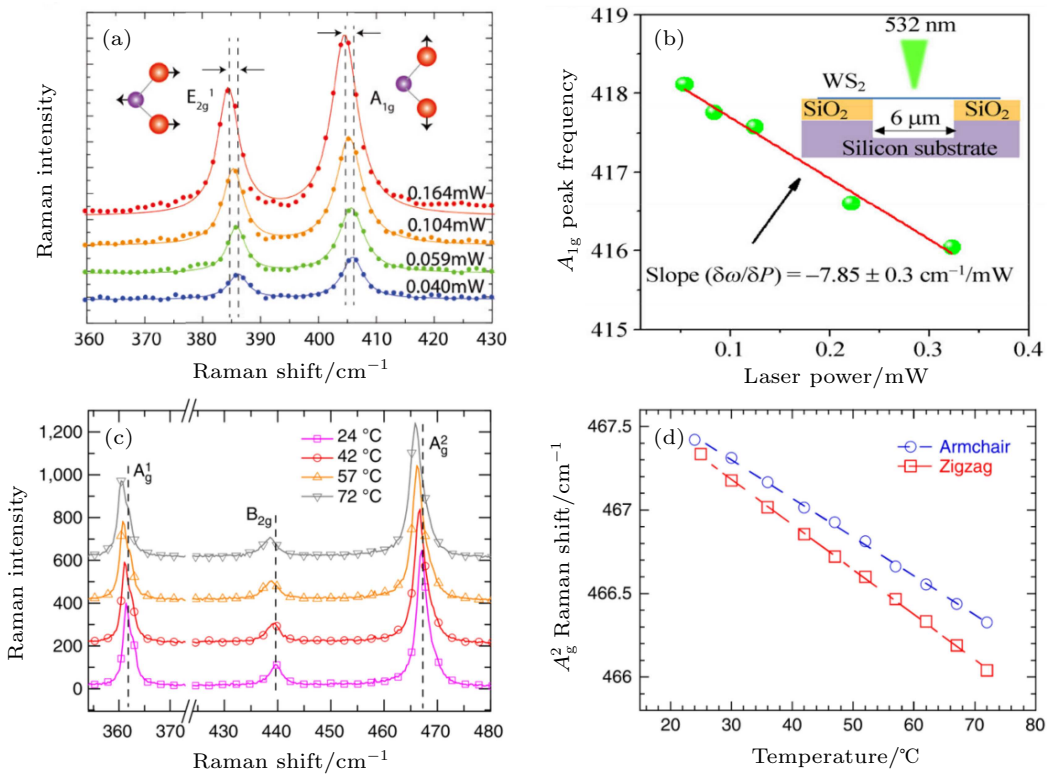


Fig. 3. (color online) Effect of laser power on Raman spectra. (a) Raman spectra of monolayer MoS_2 for different values of laser power. Both the E^1_{2g} and A_{1g} modes redshift as the laser power increases. Reproduced with permission from Ref. [64]. Copyright 2014, American Chemical Society. (b) The A_{1g} mode of WS_2 redshifts with the increasing laser power. Reproduced with permission from Ref. [67]. Copyright 2013, Springer International Publishing. (c) Raman spectra of armchair-edged BP with polarized laser excitation under different temperatures of 24 °C, 42 °C, 57 °C, and 72 °C, respectively. The vibrational modes A^2_g, B_{2g}, and A^1_g are redshifted with the increase of the laser power. (d) Raman shift of the A^2_g mode as a function of temperature for both armchair- and zigzag-edged BP under polarized laser excitation. Open circles and rectangles indicate armchair- and zigzag-edged BP under polarized laser excitation, respectively. Reproduced with permission from Ref. [68]. Copyright 2015, Nature Publishing Group.

2.3. Effect of strain

The degree of orbital interactions, mechanical properties, and electronic band dispersion of ultrathin materials are sensitive to strain. Raman scattering is an efficient tool to probe the strain applied to few-layer and monolayer 2D material films. In recent years, there have been many reports studying uniaxial and biaxial strain applied to few-layer materials theoretically and experimentally.[69–83] Usually, strain is induced by bending the flexible substrates supporting 2D materials. In-

plane mode such as E_{2g} is sensitive to external stimuli and split into two modes when the strain approaches the critical value, indicating the emergence of broken symmetry. Huang *et al.*[81] reported that the 2D peak of single-layer graphene is split into two modes ($2D^+$ and $2D^-$) under uniaxial strain of up to $\sim 4\%$. The uniaxial strain is applied to graphene with a three-point bending method by bending the flexible PDMS substrate. The intensities of the two modes depend on the laser polarization and the sample orientation. Desai *et al.*[84] found that the E^1_{2g} mode of WSe_2 (1–4 layers) splits into two peaks under uniaxial tensile strain of up to $\sim 2\%$. The peak splitting increases as the strain increases. The uniaxial tensile strain is applied on the sample with a two-point bending method by directly bending the flexible polyethylene terephthalate glycol-modified (PETG) substrate. Wang *et al.*[85] found that the E^1_{2g} mode of monolayer MoS_2 redshifts with the increasing strain and splits into two modes under uniaxial strain up to 1%. Zhu *et al.*[86] studied the uniaxial tensile strain applied to monolayer and bilayer MoS_2. The employed apparatus for applying strain to MoS_2 is shown in Fig. 4(a). Uniaxial strain can be successfully applied to MoS_2 by bending the flexible polyethylene terephthalate (PET) substrate due to the van der Waals attraction between the sample and the substrate. As seen in Fig. 4(b), the E' and E^1_{2g} modes split into $A'(1)/A'(2)$ and $A_g(1)/A_g(2)$ peaks, respectively. This indicates that the isotropic symmetry of MoS_2 in the *xy*-plane has been broken. The A' and A_{1g} modes barely shift with the increasing applied strain, illustrating that the vibration along the *c*-axis is not sensitive to tensile strain. By using the same method, Lloyd *et al.*[87] studied the continuous and reversible tuning of the optical bandgap of a suspended monolayer MoS_2 film by applying biaxial strain. As seen from Fig. 4(c), the A_{1g} and E^1_{2g} modes both soften (redshift) with the increasing strain. However, the peak positions of 2L and 3L MoS_2 shift less than in the case of the monolayer. The redshifts of the Raman peaks with the increasing tensile strain in the described reports can be attributed to the reduction of the force constants in the 2D material flake. The atom bond length increases under tensile strain. Hui *et al.*[88] found that both the A_{1g} and E^1_{2g} blueshift as the piezoelectricity-induced biaxial compressive strain increases (Fig. 4(d)). The blueshift of the Raman peaks can be attributed to the increase of the force constants. The atom bond length decreases under compressive strain. In addition, TMDs are more sensitive to the biaxial than uniaxial strain.[83]

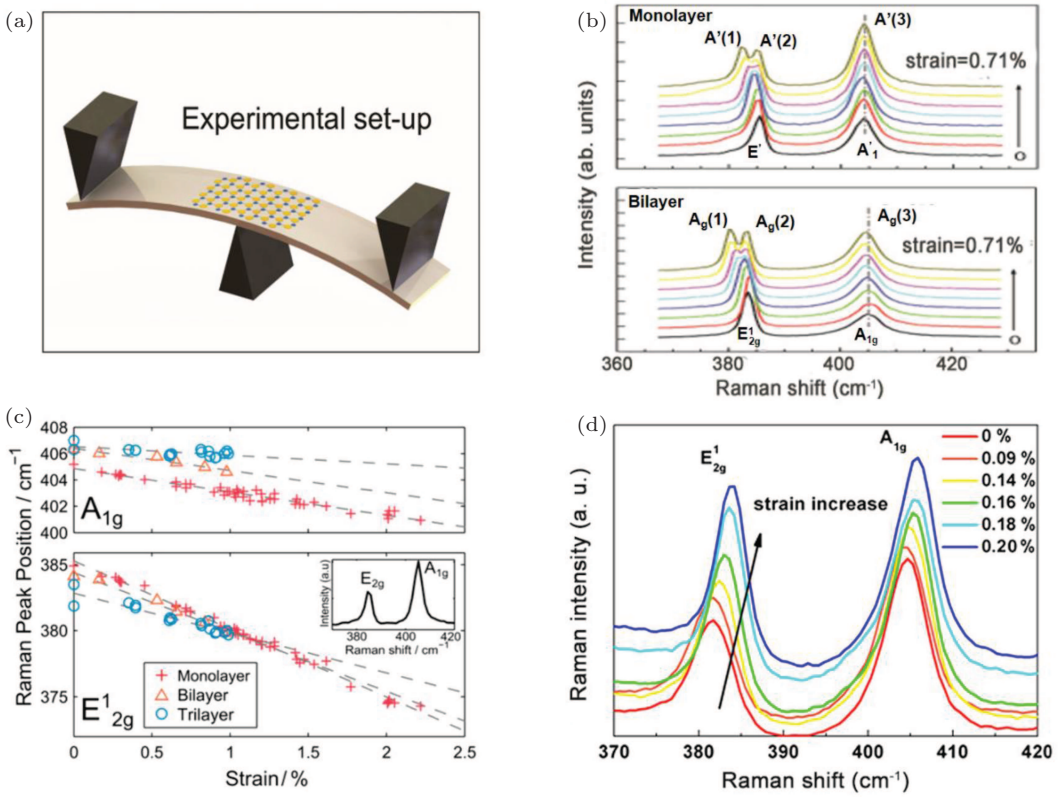


Fig. 4. (color online) Effect of strain on MoS_2 films and their Raman signals. (a) Schematic of the three-point bending method for strain measurement. (b) Raman spectra for mono- and bilayer MoS_2 with strain applied. The $E'(E^1_{2g})$ mode splits into two modes under the applied tensile strain. Reproduced with permission from Ref. [86]. Copyright 2013, American Physical Society. (c) Peak positions of the E^1_{2g} and A_{1g} modes as functions of biaxial strain for 1L, 2L, and 3L MoS_2. The inset shows the E^1_{2g} and A_{1g} Raman modes of unstrained MoS_2. Reproduced with permission from Ref. [87]. Copyright 2016, American Chemical Society. (d) Raman spectra of trilayer MoS_2 under varying compressive strain. Both the E^1_{2g} and A_{1g} modes blueshift for the compressive strain increasing from 0 to 0.2%. Reproduced with permission from Ref. [88]. Copyright 2013, American Chemical Society.

2.4. Effect of substrates

The interaction between the substrate and 2D materials varies depending on the type of substrate material. There are several reports studying the effects of substrates on 2D materials.[47,89,90] Buscema *et al.*[89] studied the differences in the parameters of MoS_2 on various conducting and insulating substrates. The results indicate that the position of the E^1_{2g} mode is insensitive to the substrate characteristics. However, the A_{1g} mode stiffens for some substrates. The intensities for both modes are different for different substrates. The stiffening of the A_{1g} mode is related to the vdW force between the 2D material flake and the substrate. For example, as the A_{1g} mode is the out-of-plane vibrational mode involving S atoms in MoS_2, the electrostatic environment changes when the motion occurs, which may affect the A_{1g} mode frequency. Shi *et al.*[91] found that the frequency difference between the A_{1g} and E^1_{2g} peaks for samples transferred on SiO_2 and quartz are smaller than that before the transfer process due to the strong interface interaction.

Banszerus *et al.*[90] found that h-BN, WSe_2, and MoS_2 are better substrates than SiO_2 and sapphire, as shown in Fig. 5. It indicates that the interaction between materials from the 2D family is smaller than for other solid-state crystal materials. Rough surfaces of $SrTiO_3$, AlN, and SU-8 are not suitable for high-quality graphene devices because these substrates introduce nanometer-scale strain variations and significant charge carrier doping in graphene. In summary, 2D materials are well suitable as substrates for graphene due to the lower values of Γ_{2D} (the FWHM of the 2D-peak) and little overall doping. At the same time, rough surfaces, especially oxides, are not suitable substrates for graphene as they introduce additional charge carrier doping.

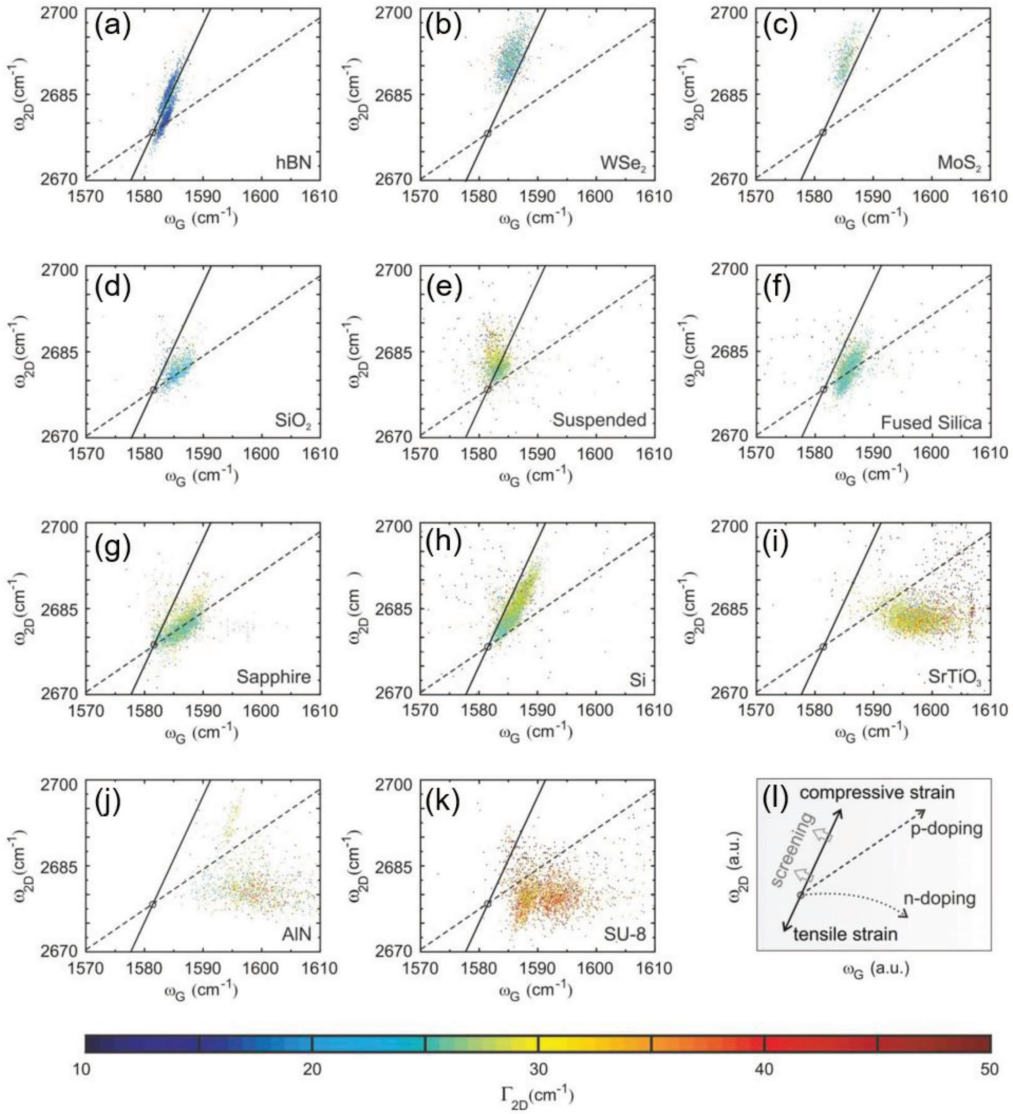


Fig. 5. (color online) Interaction of graphene with different substrates including various 2D materials. (a)–(k) Scatter diagrams of ω_{2D} versus ω_G acquired from the spatially resolved Raman maps on different substrates. The black solid lines represent the strain axes and the black dashed lines represent the doping axes. The black circles indicate the point corresponding to unstrained graphene. (l) Schematic of the influence of strain and strain-induced p- and n-doping on ω_{2D} and ω_G. Reproduced with permission from Ref. [90]. Copyright 2017, IOP Publishing.

2.5. Thickness identification

The properties of 2D materials depend on the number of layers. For example, bulk MoS_2 has an indirect bandgap, which transforms into a direct bandgap in monolayer MoS_2. It is necessary to identify the number of layers of 2D materials. Atomic force microscopy, optical contrast, and Raman spectroscopy have been widely used to determine the number of layers of 2D materials. Among them, Raman spectroscopy is a rapid, non-destructive, and direct tool to identify the number of layers.

Different numbers of layers of 2D materials are associated with different Raman spectra. In recent years, there have been many reports on the identification of the thickness of 2D materials with Raman spectroscopy.[48,56,92–102] High- and low-frequency Raman modes are mainly found in Raman spectra. The high-frequency modes are usually associated with in-plane and out-of-plane vibrations, such as the G mode (in-plane vibration of sp^2 carbon atoms) and out-of-plane 2D mode (stacking order) in layered graphene or the E^1_{2g} mode (in-plane vibration of M and X atoms) and A_{1g} mode (out-of-plane vibration of X atoms) in MX_2. The intensities of the in-plane R modes are independent on the angle θ (the polarization of the incident light and scattered photons), while θ affects the intensity of the out-of-plane modes.[26] Generally speaking, the frequency of the E^1_{2g} mode redshifts, and that of the A_{1g} mode blueshifts with the increasing number of layers in layered MX_2.[30,53,93,103,104] Zhao *et al.*[93] reported that the A_{1g} mode blueshifts, and the E^1_{2g} mode redshifts when the number of layers increases for both WS_2 and WSe_2 films. The FWHMs of the two modes decrease with the increasing thickness. Since the interlayer vdW forces suppress atomic vibrations as the thickness increases, the out-of-plane A_{1g} mode blueshifts with the increasing number of layers. The redshift of E^1_{2g} is associated with the structural changes or the increase of the long-range Coulomb force in interlayer interactions.[30] However, the typical Raman modes of WS_2 are less sensitive to the number of layers.[27,52] Additionally, the frequency difference ($\Delta\omega$) between the A_{1g} and E^1_{2g} modes can be used to identify few-layer MX_2 (when the number of layers is less than 6).[55] The $\Delta\omega$ of the two modes is calculated as $\Delta\omega(A-E) = \mathrm{Pos}(A_{1g}) - \mathrm{Pos}(E^1_{2g}) = 25.8 - 8.4/N\,(1 < N < 6)$.[55] Yu *et al.*[48] found that the frequency difference between the A_{1g} and E_{2g} peaks for a MoS_2 film increases with the increase of the thickness. Li *et al.*[105] reported the high-frequency Raman spectra of MoS_2 with 1–120 layers, as shown in Fig. 6(a). They found that the curve of the peak intensity as a function of thickness is not monotonous, and a new enhanced peak appears at ~ 85 layers. The increased intensities of the peaks are due to interference effects.

The restoring forces of the high-frequency Raman vibrational modes are dominated by the interaction associated with strong chemical bonds. The differences for high-frequency Raman modes are not very obvious as N increases. In contrast, the difference for the low-frequency Raman modes is more pronounced for different numbers of layers.

The low-frequency modes correspond to interlayer vibrations where each layer moves as a whole unit. This motion could be either perpendicular or parallel to the layers.[18,106,107] There are two types of interlayer vibration modes, the shear (S) mode, where the oscillation is parallel to the layer plane, and the layer-breathing (LB) mode, where the oscillation is perpendicular to the layer plane,[49] arising from the Davydov splitting of the zero-frequency acoustic modes.[26] The shear mode is also called C mode in some papers.[18,106] The LB mode is also known as the compression vibrational mode.[18,61,108] Since the interlayer coupling in TMDs is associated with the weak vdW interaction, the frequencies of the LB and S modes are usually lower than 100 cm^{-1}.[52,108,109] In bulk MX_2, the LB mode is defined as B^2_{2g} and is optically inactive. The S mode is defined as E^2_{2g} with the adjacent layers vibrating out-of-phase, which is Raman active. In MX_2 with an odd number of layers, the S modes are defined as E'' (R) and E' (IR + R), and the LB modes are defined as A'_1 (R) and A''_2 (IR). In MX_2 with an even number of layers, the S modes are E_g (R) and E_u (IR), and the LB modes are A_{1g} (R) and A_{2u} (IR). The S and LB modes do not exist in monolayer 2D materials due to their interlayer coupling properties. The S and LB modes are not detectable in the bulk layered materials with only one rigid layer in its unit cell (for example, ReS_2, $ReSe_2$, and Bi_2Se_3).[52] The intensities of the S and LB modes are determined by the associated electron–phonon coupling effect. In NL 2D materials, there are N−1 doubly degenerate interlayer S modes and N−1 LB modes. The frequencies of the S and LB modes depend on the following equations ((1) for S and (2) for LB):[52,109]

$$\mathrm{Pos}(S_{NN-i}) = \sqrt{2}\mathrm{Pos}(S_{21})\cos(i\pi/2N), \quad i = 1,2,\ldots,N-1, \tag{1}$$

$$\mathrm{Pos}(\mathrm{LB}_{NN-i}) = \sqrt{2}\mathrm{Pos}(\mathrm{LB}_{21})\cos(i\pi/2N), \quad i = 1,2,\ldots,N-1. \tag{2}$$

$\mathrm{Pos}(S_{21})$ and $\mathrm{Pos}(\mathrm{LB}_{21})$ are the S and LB frequencies of 2L 2D materials flakes.[52] Low-frequency Raman spectroscopy is a direct, substrate-free and precise tool to identify the number of layers in few-layer 2D materials. The low-frequency Raman spectra of MoS_2 with 1–19 layers are shown in Fig. 6(b).[55] The authors demonstrated that the C mode stiffens from ~ 22.6 cm^{-1} in 2L to 32.5 cm^{-1} in 19L-MoS_2, while the LB mode softens from ~ 40.1 cm^{-1} in 2L to 4.7 cm^{-1} in 19L-MoS_2. Most related materials exhibit similar Raman shifts: the LB modes soften, and the S modes stiffen when the number of layers increases; this is

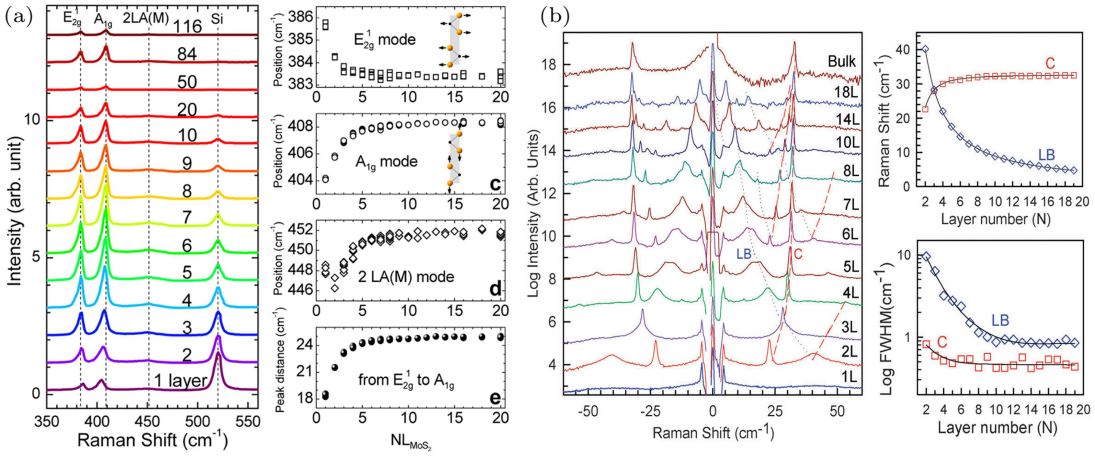


Fig. 6. (color online) High- and low-frequency Raman spectra of MoS_2 with various thickness. (a) Typical Raman spectra of 1L to bulk MoS_2 (left), and the positions of the E^1_{2g}, A_{1g}, and $2\times$LA(M) Raman modes as functions of NL. Reproduced with permission from Ref. [105]. Copyright 2012, American Chemical Society. (b) Stokes and anti-Stokes Raman spectra of MoS_2 with various thickness in a range from -60 to 60 cm^{-1} (left), and the frequency and FWHM of the C and LB modes as functions of the number of layers (right). Reproduced with permission from Ref. [18]. Copyright 2013, American Physical Society.

characteristic for WSe_2,[56] $MoTe_2$,[26] $NbSe_2$,[110] $MoSe_2$,[53] $Mo_{0.5}W_{0.5}S_2$ alloy,[106] and MoS_2.[61] Particularly, different stacking order results in different trends of low-frequency Raman modes. For example, the S mode of AB-stacked few-layer graphene (FLG) stiffens with the increasing number of layers, while that of ABC-stacked FLG softens.[107] The LB modes soften with the increasing number of layers for both isotropic and anisotropic stacking of NL ReS_2, while the S modes stiffen for isotropic stacking of NL ReS_2 and soften for anisotropic stacking of NL ReS_2 as the number of layers increases.[111]

3. Applications of Raman spectroscopy

Raman spectroscopy analysis is widely used in many application fields. Here, we mainly discuss the applications of Raman scattering for semiconductors, superconductivity, photoelectricity, and thermoelectricity.

3.1. Raman scattering in semiconducting devices

Since the discovery of the novel physical properties and bandgap structures of 2D materials, many 2D-materials-based semiconducting devices emerged. Raman spectroscopy is an effective tool to study the carrier concentration in 2D-materials-based semiconducting devices. Das *et al.*[112] studied Raman scattering in a top-gated graphene transistor. The results show that the G peak redshifts when the top-gate voltage (V_{TG}) increases from -2.2 V to 0.6 V and then blueshifts for the voltages from 0.6 V to 4.0 V. The Raman shift of the G peak increases for both hole doping and electron doping. However, the 2D peak decreases for V_{TG} below 3 V for electron doping. The FWHM of the G peak decreases for both hole doping and electron doping. This result indicates that the

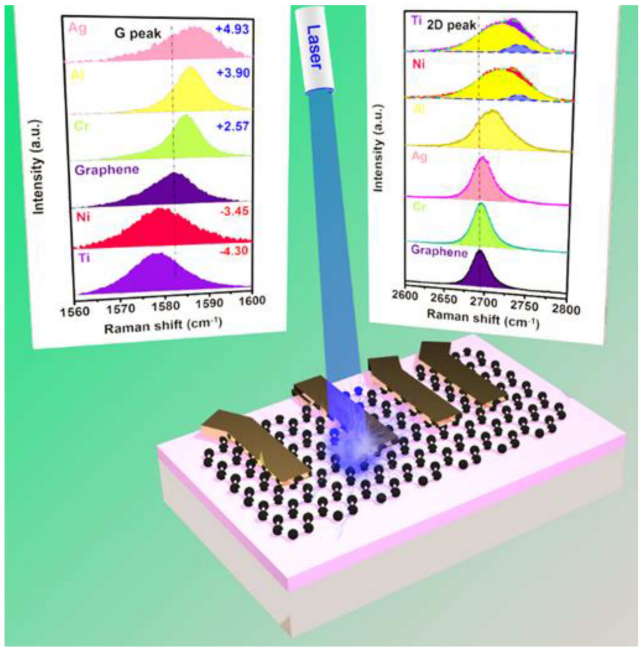


Fig. 7. (color online) Properties of graphene metal contact probed by Raman spectroscopy. Reproduced with permission from Ref. [114]. Copyright 2018, Elsevier.

dependence of the G mode on V_{TG} is weaker than that of the 2D mode. For TMDs, the $A_{1g}(A'_1)$ modes are more sensitive to V_{TG} than the $E^1_{2g}(E')$ modes. Since the $A_{1g}(A'_1)$ mode is the out-of-plane vibrational mode of X atoms, it is sensitive to surface adsorption and doping. Therefore, all electronic states introduce a perturbation to the $A_{1g}(A'_1)$ mode due to relatively strong large electron–phonon coupling. For example, Chakraborty *et al.*[113] studied the effect of carrier concentration on Raman scattering in a single-layer MoS_2 top-gated FET. The A'_1 mode significantly redshifts when V_{TG} increases from 0 to 2.0 V, whereas the E' mode remains almost unchanged. Miller *et al.*[65] found that the A_{1g} modes of 1L

and 2L MoS_2 redshift as V_{TG} increases from −1.0 to 1.0 V. However, the E^1_{2g} mode changes only slightly in monolayer and negligibly in bilayer MoS_2 with the increasing V_{TG}. Xu *et al.*[114] studied the properties of graphene contacted with various metals using Raman spectroscopy. Figure 7 shows the resulting Raman spectra of the graphene characteristic peaks. Chemisorbed metals Ni and Ti not only cause a dramatic blueshift of the 2D peak but also broaden it and transform into a sum of two Gaussians. Thus, the lowest contact resistivity of $\sim 6.8 \times 10^{-5}$ Ω·cm^{-2} is measured when metal Ni is used as an electrode material in a graphene FET.

3.2. Raman scattering in superconductivity

A charge density wave (CDW) is a symmetry-reducing ground state with periodic modulations of charge densities and the associated lattice distortions in layered materials.[31,115] CDWs are affected by electron–phonon interactions, Peierls instabilities, and fluctuation effects from finite temperatures and disorders.[31] vdW materials provide an ideal platform to study CDWs and the associated superconductivity.[25,31,115] Raman spectroscopic measurement is an effective tool to identify the transition temperature of the CDW phase. Goli *et al.*[115] found that the temperature of the transition to the CDW phase of $TiSe_2$ can increase up to ∼ 240 K when the thickness is decreased to below ∼ 100 nm. They found a new mode appearing at ∼ 460 cm^{-1} below 200 K in bulk $TiSe_2$. Hajiyev *et al.*[30] found that the two-phonon peaks for 1L, 2L, and bulk $TaSe_2$ soften with increasing temperature, and the frequency of this mode exhibits a sudden drop at 120 K. It indicates that the temperature of the transition from the metallic phase to ICDW (incommensurate charge density wave) phase of 2H-$TaSe_2$ is ∼ 120 K. Xi *et al.*[31] found that both the CDW and the superconducting phase exist down to the monolayer limit. The superconducting transition temperature decreases with decreasing thickness. However, the CDW transition temperature increases from 33 K in bulk to 145 K in a monolayer. The temperature dependence of Raman spectra for bulk, bilayer, and monolayer $NbSe_2$ are shown in Fig. 8. The soft mode of bulk $NbSe_2$ redshifts with decreasing temperature and stops changing when the temperature is down to 33.5 K (T_{CDW}). There are two new Raman modes emerging when the temperature is below T_{CDW}. One mode appears at ∼ 35 cm^{-1}, where the CDW fluctuations are strong, with frequency and intensity both dropping rapidly to zero when the temperature is increasing and approaching T_{CDW} due to the second-order phase transition. The other new mode is at ∼ 190 cm^{-1}. The frequency of this mode is independent of the number of layers N, whereas the frequency at zero temperature blueshifts for decreasing thickness. Both modes persist at much higher temperatures, indicating the higher associated CDW transition temperatures. This result shows that there is a strongly enhanced CDW order in atomically thin $NbSe_2$ driven by strong electron–phonon coupling. In summary, the sudden drops of the Raman mode intensities and emerging of the new Raman modes are characteristic for the CDW phase.

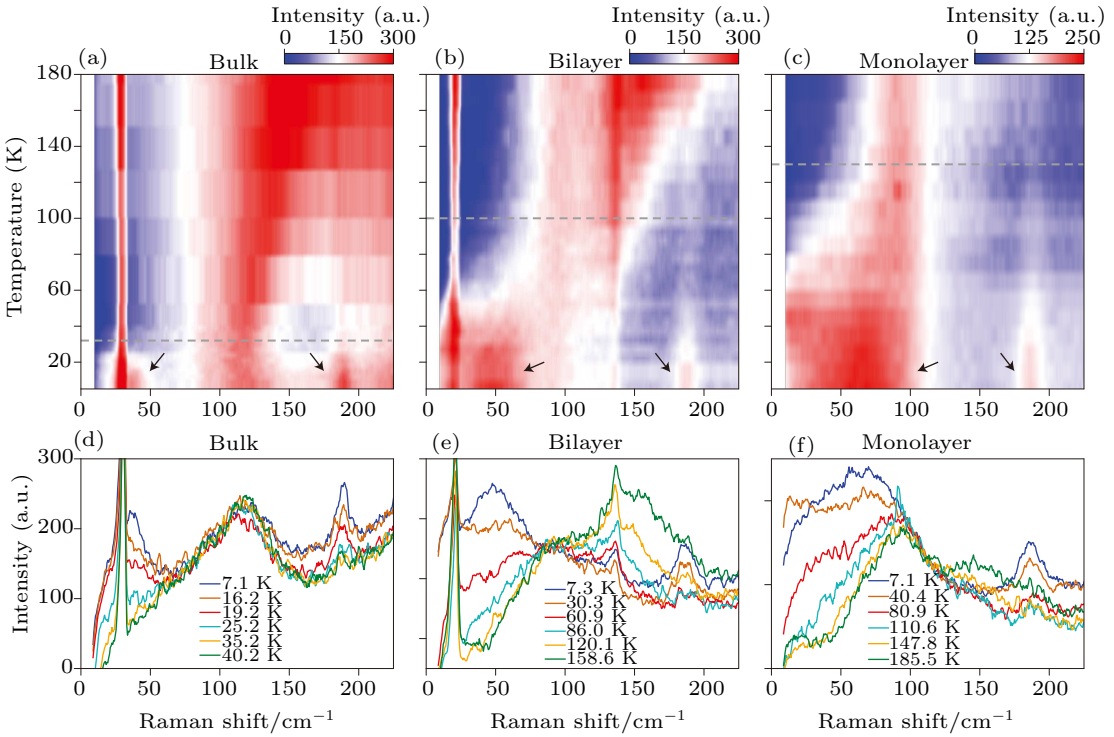


Fig. 8. (color online) Raman study of CDW phenomena in 2D materials. (a)–(c), Temperature maps of the Raman scattering intensity of bulk, 2L, and 1L NbSe2, respectively, for the perpendicular polarization configuration. The two arrows in each map indicate the low-frequency feature and the weak high-frequency feature. Dashed lines approximately indicate TCDW. (d)–(f) Raman spectra of each sample at selected temperatures. Reproduced with permission from Ref. [31]. Copyright 2015, Nature Publishing Group.

3.3. Raman scattering for studying thermoelectricity

Temperature-dependent Raman spectroscopy is an efficient tool to investigate the thermoelectrical properties of 2D materials.[116–118] Sahoo *et al.*[119] studied the thermal conductivity of few-layer MoS_2 by Raman spectroscopy. The schematic for the heat conduction process in suspended few-layer MoS_2 is shown in Fig. 9(a). Figure 9(b) demonstrates that both the A_{1g} and E^1_{2g}modes redshift as the temperature increases from 83 to 473 K under the 532 nm laser excitation. The observed data for the Raman peak positions versus temperature were fitted using the Grüneisen model[116,120]

$$\omega(T) = \omega_0 + \chi T, \tag{3}$$

where ω_0 is the frequency of the Raman mode at 0 K, and χ is the first-order temperature coefficient of the relative Raman mode. T stands for the changed temperature. The first-order temperature coefficient corresponds to the slope of the Raman mode as a function of temperature. The FWHM of A_{1g} in few-layer MoS_2 decreases as the temperature increases from 83 to 523 K (Fig. 9(c)). The A_{1g} mode is selected for the evaluation of the thermal conductivity because the intensity of the A_{1g}mode is much higher than that of the E^1_{2g} mode. The thermal conductivity is calculated by the authors as follows:

$$k = \chi_{A_{1g}} \left(\frac{1}{2\pi h}\right) \left(\frac{\delta w}{\delta P}\right)^{-1}. \tag{4}$$

Here, $\chi_{A_{1g}}$ is the first-order temperature coefficient for the A_{1g} mode, and $\frac{\delta w}{\delta P}$ is the change of the A_{1g} frequency with the incident laser power. The parameter h represents the thickness of the sample (6.5 nm in the reported work). The value of $\frac{\delta w}{\delta P}$ obtained from the slope of the laser-power-dependent A_{1g} (Fig. 9(d)) is 5.7 cm^{-1}/mW. The first-order temperature coefficient for the A_{1g} mode is -1.23×10^{-2} cm^{-1}/K, as seen in Fig. 9(a). The thermal conductivity of the few-layer MoS_2 sample is $\sim$ 52 W/mK calculated using Eq. (2) and the existing data. Yan *et al.*[64] found that both the A_{1g} and E^1_{2g} modes of exfoliated monolayer MoS_2 also redshift with increasing temperature (for 514.5 nm laser wavelength). However, the thermal conductivity was evaluated to be $\sim$ 34.5 W/mK, which is smaller than the result of Sahoo *et al.* ($\sim$ 52 W/mK), where the MoS_2 sample was prepared by chemical vapor deposition. Thripuranthaka *et al.*[117] found that the A_{1g} and E^1_{2g} Raman peak positions for single-layer WS_2 redshift when the temperature increases from 77 to 623 K under the 514.5 nm laser excitation. The behavior of Raman modes for varying temperature is similar to the case of MoS_2. Zhang *et al.*[121] studied the low-temperature Raman response of few-layer BP and found that the A^1_g, A^2_g, and A_{1g} vibration modes stiffen as the temperature decreases from 20 to -160 °C. They also found that, for few-layer phosphorene, the Raman shift is more sensitive to temperature than for graphene and MoS_2 due to the mechanical flexibility of phosphorene. Xia *et al.*[122] reported that the Raman modes of anisotropic 2D SnS flakes blueshift when the temperature decreases from 25 °C to -195 °C under the 532 nm laser excitation. It is interesting that the result

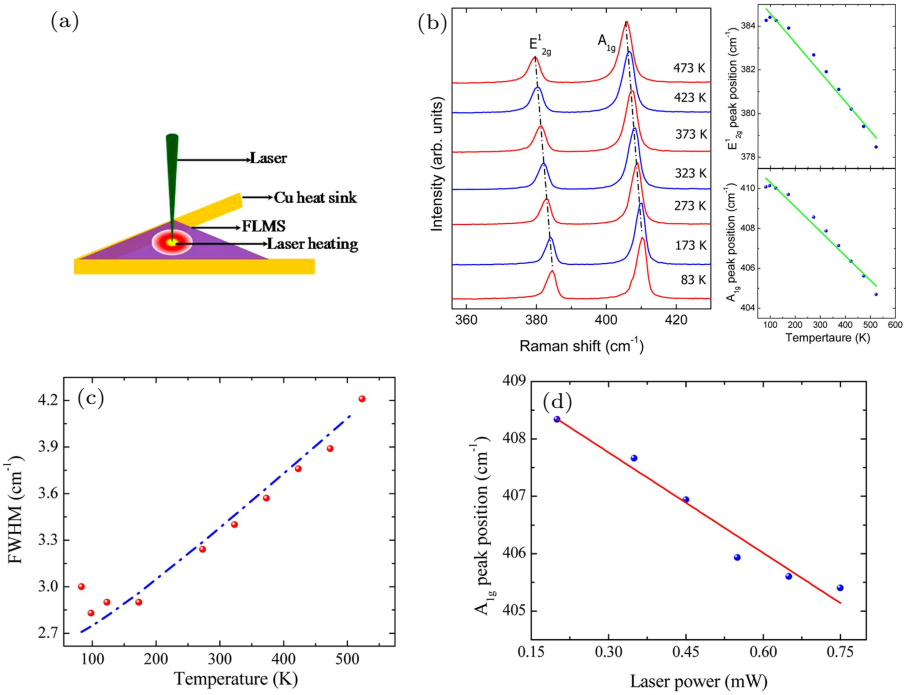


Fig. 9. (color online) Raman study of thermoelectricity in 2D materials. (a) Schematic for the heat conduction process in suspended few-layer MoS_2. (b) Raman spectra of suspended few-layer MoS_2 at different temperatures (left). The A_{1g} and E^1_{2g} peak positions as functions of temperature (right). Both modes redshift as the temperature increases. (c) FWHM of the A_{1g} peak as a function of temperature. The FWHM increases as the temperature increases. (d) The A_{1g} mode frequency as a function of laser power. Redshifts are found as the temperature increases. Reproduced with permission from Ref. [119]. Copyright 2013, American Chemical Society.

demonstrates that 2D SnS flakes exhibit a higher temperature sensitivity than black phosphorus (BP). Pawbake *et al.*[120] found that the Raman peaks of titanium trisulfide (TiS_3) shift toward lower frequencies when the temperature increases from 88 K to 570 K. All the results described above prove that the frequencies of typical Raman modes could be used to study the thermal conductivity of 2D materials in a non-destructive way. Chen *et al.*[123] applied an AC lock-in technique and successfully separated the thermoelectric voltage (ΔV) in a graphene/hBN/graphene heterostructure device. The Raman 2D and G peaks shift with temperature at a rate of -0.057 cm^{-1}/K and -0.022 cm^{-1}/K, respectively.[124] The shifts of the 2D and G peaks are converted to the temperature gradient (ΔT). Then, the Seebeck coefficent ($S = \Delta V/\Delta T$) of -99.3 μV/K is obtained.

3.4. Raman scattering for studying photoelectricity

Combining materials with different work functions can generate photoexcited electrons and holes accumulated in different layers.[125] The p–n junction devices are implemented by bringing p-doped and n-doped materials in contact. vdW heterostructures, which consist of different 2D materials held together by weak vdW forces, have wide applications in photovoltaic devices. The carrier transport in vdW heterostructures is dominated by the interfacial properties of the adjacent layers with lattice mismatch. The interlayer coupling, charge transfer, lattice vibrations, and interface diffusion in vdW heterostructures transform the band structure, shift the Fermi level, and introduce band offsets.[55] The low-frequency Raman spectroscopy is a powerful tool to detect the interlayer coupling and polytypes of heterostructures because the S and LB modes are sensitive to the stacking order.

There have been many reports on vertical and in-plane heterostructures in recent years.[101,126–137] Zhang *et al.*[127] studied vertical MoS_2/WS_2 heterostructures with AA and AB stacking grown by chemical vapor deposition (CVD) and vertical MoS_2/WS_2 heterostructures obtained with the transfer technique. The structure of CVD-prepared MoS_2/WS_2 heterostructures is associated with more efficient interlayer charge transfer and spatially separated exciton recombination than the mechanically transferred heterostructures, which due to the strong coupling. Figure 10(a) shows the typical Raman modes of CVD-grown MoS_2/WS_2 heterostructures. As seen from Fig. 10(b), the Raman spectra of mechanically transferred MoS_2/WS_2 heterostructures show a simple superposition of the individual Raman modes of WS_2 and MoS_2, whereas the A_{1g} modes of CVD-grown MoS_2/WS_2 heterostructures blueshift by 3–4 cm^{-1} comparing with the modes of WS_2 and MoS_2. This reveals strong interlayer coupling in the CVD-grown MoS_2/WS_2 heterostructures. As seen from Fig. 10(c), the frequency of the LB mode of an AB-stacked heterostructure is ~ 2 cm^{-1} higher than that of an AA-stacked heterostructure. This may be due to the shorter

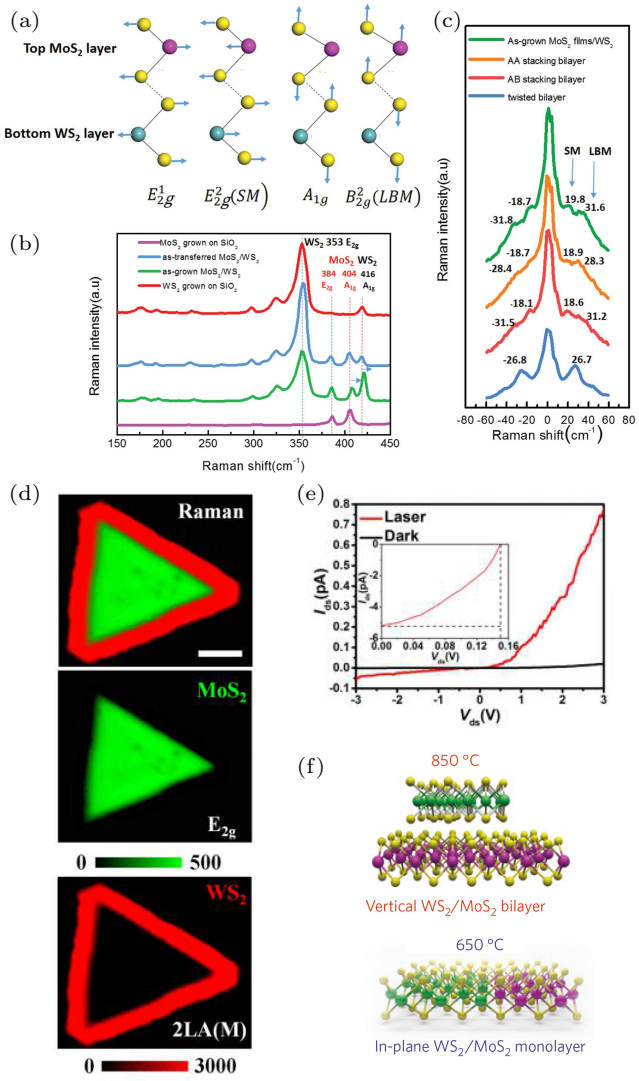


Fig. 10. Raman study on a 2D heterostructure as a photovoltaic device. (a) Raman vibrational modes of a vertical bilayer WS_2/MoS_2 heterostructure. (b) Raman spectra of as-grown 1L WS_2 and MoS_2 and as-grown, as-transferred WS_2/MoS_2 heterostructures. (c) Raman spectra of the LB and S modes for as-grown MoS_2 films on WS_2, AA stacked, AB stacked, and transferred twisted stacked MoS_2/WS_2 heterostructures, respectively. Reproduced with permission from Ref. [127]. Copyright 2016, Wiley-VCH Verlag GmbH & Co. KGaA. (d) Raman mapping results for lateral WS_2/MoS_2 heterostructures, MoS_2, and WS_2, respectively. (e) I–V curve of a lateral WS_2/MoS_2 heterostructure diode in the dark (black line) and under illumination with a wavelength of 514 nm and power of 1 mW (red line). Inset shows the photovoltaic effect. Reproduced with permission from Ref. [138]. Copyright 2015, American Chemical Society. (f) Schematic of vertical and lateral WS_2/MoS_2 heterostructures. Reproduced with permission from Ref. [136]. Copyright 2014, Nature Publishing Group.

interlayer distance and stronger interlayer coupling of AB-stacked heterostructures compared to AA-stacked heterostructures. Moreover, the vibrational frequency of the LB mode of an as-grown AB stacked MoS_2/WS_2 heterostructure is 2–4 cm^{-1} higher than that of a transferred twist MoS_2/WS_2 heterostructure, demonstrating the weak interlayer coupling and lower packing efficiency of the transferred twist heterostructure. In comparison, the S modes can be observed only when heterostructures have perfect commensurate stacking due to the restoring force of the lateral displacement. In addition to vertical heterostructures, Chen *et al.*[138] studied lateral

MoS_2/WS_2 heterostructures prepared by the CVD method. The obtained Raman mapping images of as-grown WS_2/MoS_2 heterostructures are shown in Fig. 10(d), which demonstrates the features of an in-plane WS_2/MoS_2 heterostructure, with a triangular monolayer MoS_2 domain as the core and WS_2 as the shell layer. Figure 10(e) shows the I_{ds}–V_{ds} curves of a p–n diode of the lateral WS_2/MoS_2 heterostructure in the dark (black line) and under illumination with a wavelength of 514 nm and power of 1 mW (red line), with the inset showing the photovoltaic effect. The open-circuit voltage V_{OC} is ~ 0.15 V, and the short-circuit current I_{SC} is ~ 5.2 pA under the laser illumination of the device. The current rectification observed in the figure indicates that there is a p–n diode formed in the WS_2/MoS_2 lateral heterostructure. The output current was found to increase with the increasing positive gate voltage under different back gate voltages of 0–80 V. This indicates that the n-type monolayer MoS_2 partly limits the charge transport in the p–n diode. Lateral heterostructures based on TMDs can dramatically enhance the performance of optoelectronic devices.[125] Gong *et al.*[136] studied both vertical and in-plane MoS_2/WS_2 heterostructures. The structures of vertical and lateral WS_2/MoS_2 heterostructures are shown in Fig. 10(f). The Raman spectra of vertical WS_2/MoS_2 heterostructures are the same as reported by Zhang *et al.* The Raman spectra of lateral WS_2/MoS_2 heterostructures are the same as reported by Chen *et al.* They show that the p–n junctions of in-plane WS_2/MoS_2 heterostructures without external electrical tuning exhibit a two orders of magnitude higher forward bias current compared to the the reverse current.

Currently, most 2D heterostructures are created by the micromechanical stacking technique with only certain combinations of interfaces, and the direct growth of heterostructures by CVD or vdW epitaxy with their own inherent limitations is not yet well developed. Therefore, further study of heterostructures is necessary.

4. Conclusion

The electronic and optical properties of 2D materials make the interlayer coupling in a multilayer structure dependent on the number of layers. We reviewed the phonon structure and symmetry of TMDs and the application of Raman spectroscopy for studying 2D materials. Raman spectroscopy is a powerful tool to investigate the fine structure, atomic bonds, and mechanical and thermal properties of 2D materials. Raman spectroscopy is expected to be an ideal tool to detect various interesting phenomena in van der Waals heterostructures fabricated by different techniques. The control of surface reconstruction, charge transfer, and built-in electric fields in vdW heterostructures is yet to be demonstrated. The interlayer vibrational modes, S and LB, will provide a useful means to study the interface coupling and layer stacking in various vdW heterostructures.

References

[1] Novoselov K S and Geim A K 2007 *Nat. Mater.* **6** 183
[2] Zhang L L, Zhou R and Zhao X S 2010 *J. Mater. Chem.* **20** 5983
[3] Novoselov K S, Geim A K, Morozov S V, Jiang D, Zhang Y, Dubonos S V, Grigorieva I V and Firsov A A 2004 *Science* **306** 666
[4] El-Kady M F, Strong V, Dubin S and Kaner R B 2012 *Science* **335** 1326
[5] Zhang D W, Li X D, Li H B, Chen S, Sun Z, Yin X J and Huang S M 2011 *Carbon* **49** 5382
[6] Balog R, Jørgensen B, Nilsson L, Andersen M, Rienks E, Bianchi M, Fanetti M, Lægsgaard E, Baraldi A and Lizzit S 2010 *Nat. Mater.* **9** 315
[7] Xia F N, Farmer D B, Lin Y M and Avouris P 2010 *Nano Lett.* **10** 715
[8] Li X M, Li T, Chen Z F, Hui F, Li X S, Wang X R, Xu J B and Zhu H W 2017 *Appl. Phys. Rev.* **4** 021306
[9] Balandin A A, Ghosh S, Bao W n, Calizo I, Teweldebrhan D, Miao F and Lau C N 2008 *Nano Lett.* **8** 902
[10] Li L K, Yu Y J, Ye G J, Ge Q Q, Ou X D, Wu H, Feng D L, Chen X H and Zhang Y B 2014 *Nat. Nanotechnol.* **9** 372
[11] Chhowalla M, Shin H S, Eda G, Li L J, Loh K P and Zhang H 2013 *Nat. Chem.* **5** 263
[12] Xu M S, Liang T, Shi M M and Chen H Z 2013 *Chem. Rev.* **113** 3766
[13] Wang Q H, Kalantar Zadeh K, Kis A, Coleman J N and Strano M S 2012 *Nat. Nanotechnol.* **7** 699
[14] Tan C L and Zhang H 2015 *Chem. Soc. Rev.* **44** 2713
[15] Chhowalla M, Liu Z F and Zhang H 2015 *Chem. Soc. Rev.* **44** 2584
[16] Zhang H 2015 *ACS Nano* **9** 9451
[17] Falmbigl M, Fiedler A, Atkins R E, Fischer S F and Johnson D C 2015 *Nano Lett.* **15** 943
[18] Zhang X, Han W P, Wu J B, Milana S, Lu Y, Li Q Q, Ferrari A C and Tan P H 2013 *Phys. Rev. B* **87** 115413
[19] Li Y L, Rao Y, Mak K F, You Y M, Wang S Y, Dean C R and Heinz T F 2013 *Nano Lett.* **13** 3329
[20] Singh D, Gupta S K, Sonvane Y, Kumar A and Ahuja R 2016 *Catalysis Science & Technology* **6** 6605
[21] Zhang J, Peng Z P, Soni A, Zhao Y Y, Xiong Y, Peng B, Wang J B, Dresselhaus M S and Xiong Q H 2011 *Nano Lett.* **11** 2407
[22] Zhang W, Rui Y, Zhang H J, Dai X and Fang Z 2010 *New J. Phys.* **12** 065013
[23] Ganatra R and Zhang Q 2014 *ACS Nano* **8** 4074
[24] Wang X l, Gong Y j, Shi G, Chow W L, Keyshar K, Ye G, Vajtai R, Lou J, Liu Z, Ringe E, Tay B K and Ajayan P M 2014 *ACS Nano* **8** 5125
[25] Pan J, Guo C, Song C, Lai X, Li H, Zhao W, Zhang H, Mu G, Bu K, Lin T, Xie X, Chen M and Huang F 2017 *J. Am. Chem. Soc.* **139** 4623
[26] Froehlicher G, Lorchat E, Fernique F, Joshi C, Molina Sanchez A, Wirtz L and Berciaud S 2015 *Nano Lett.* **15** 6481
[27] Terrones H, Del Corro E, Feng S, Poumirol J M, Rhodes D, Smirnov D, Pradhan N R, Lin Z, Nguyen M A, Elias A L, Mallouk T E, Balicas L, Pimenta M A and Terrones M 2015 *Sci Rep.* **4** 4215
[28] Lei J Q, Liu K, Huang S, Mao X C, Hou B S, Tan J and Zhou X L 2017 *Chem. Phys. Lett.* **687** 250
[29] Zhang Z, Niu J, Yang P, Gong Y, Ji Q, Shi J, Fang Q, Jiang S, Li H, Zhou X, Gu L, Wu X and Zhang Y 2017 *Adv. Mater.* **29** 1702359
[30] Hajiyev P, Cong C, Qiu C and Yu T 2013 *Sci Rep.* **3** 2593
[31] Xi X, Zhao L, Wang Z, Berger H, Forro L, Shan J and Mak K F 2015 *Nat. Nanotechnol.* **10** 765
[32] Zhang X, Tan Q H, Wu J B, Shi W and Tan P H 2016 *Nanoscale* **8** 6435
[33] Coleman J N, Lotya M, O'Neill A, Bergin S D, King P J, Khan U, Young K, Gaucher A, De S and Smith R J 2011 *Science* **331** 568
[34] Tsai M L, Su S H, Chang J K, Tsai D S, Chen C H, Wu C I, Li L J, Chen L J and He J H 2014 *ACS Nano* **8** 8317
[35] Lin J D, Zhong J Q, Zhong S, Li H, Zhang H and Chen W 2013 *Appl. Phys. Lett.* **103** 063109
[36] Yu S H, Lee Y B, Jang S K, Kang J Y, Jeon J W, Lee C G, Lee J Y, Kim H J, Hwang E Y and Lee S J 2014 *ACS Nano* **8** 8285
[37] Bernardi M, Palummo M and Grossman J C 2013 *Nano Lett.* **13** 3664
[38] Sundaram R S, Engel M, Lombardo A, Krupke R, Ferrari A C, Avouris P h and Steiner M 2013 *Nano Lett.* **13** 1416
[39] Tao L Q, Wang D Y, Jiang S, Liu Y, Xie Q Y, Tian H, Deng N Q, Wang X F, Yang Y and Ren T L 2016 *J. Semicond.* **37** 041001
[40] Lou Z, Liang Z Z and Shen G Z 2016 *J. Semicond.* **37** 091001
[41] Xia F N, Wang H, Xiao D, Dubey M D and Ramasubramaniam A 2014 *Nat. Photonics* **8** 899

[42] Zhang Y J, Oka T, Suzuki R, Ye J T and Iwasa Y 2014 *Science* **344** 725
[43] Mak K F, McGill K L, Park J and McEuen P L 2014 *Science* **344** 1489
[44] Cao T, Wang G, Han W P, Ye H Q, Zhu C R, Shi J R, Niu Q, Tan P H, Wang E G and Liu B L 2012 *Nat. Commun.* **3** 887
[45] Zeng H L, Dai J F, Yao W, Xiao D and Cui X D 2012 *Nat. Nanotechnol.* **7** 490
[46] Kim S, Konar A, Hwang W S, Lee J H, Lee J Y, Yang J H, Jung C H, Kim H G, Yoo J B and Choi J Y 2012 *Nat. Commun.* **3** 1011
[47] Xia J, Huang X, Liu L Z, Wang M, Wang L, Huang B, Zhu D D, Li J J, Gu C Z and Meng X M 2014 *Nanoscale* **6** 8949
[48] Yu Y, Li C, Liu Y, Su L, Zhang Y and Cao L 2013 *Sci Rep.* **3** 1866
[49] Plechinger G, Heydrich S, Eroms J, Weiss D, Schüller C and Korn T 2012 *Appl. Phys. Lett.* **101** 101906
[50] Malard L M, Pimenta M A, Dresselhaus G and Dresselhaus M S 2009 *Phys. Rep.* **473** 51
[51] Ferrari A C and Basko D M 2013 *Nat Nanotechnol.* **8** 235
[52] Li X L, Han W P, Wu J B, Qiao X F, Zhang J and Tan P H 2017 *Adv. Funct. Mater.* **27** 1604468
[53] O'Brien M, McEvoy N, Hanlon D, Lee K, Gatensby R, Coleman J N and Duesberg G S 2015 *Phys. Status Solidi B* **252** 2385
[54] Wilson J A and Yoffe A D 1969 *Adv. Phys.* **18** 193
[55] Zhang X, Qiao X F, Shi W, Wu J B, Jiang D S and Tan P H 2015 *Chem. Soc. Rev.* **44** 2757
[56] Zhao Y, Luo X, Li H, Zhang J, Araujo P T, Gan C K, Wu J, Zhang H, Quek S Y, Dresselhaus M S and Xiong Q 2013 *Nano Lett.* **13** 1007
[57] Sankar R, Narsinga Rao G, Muthuselvam I P, Butler C, Kumar N, Senthil Murugan G, Shekhar C, Chang T R, Wen C Y, Chen C W, Lee W L, Lin M T, Jeng H T, Felser C and Chou F C 2017 *Chem. Mater.* **29** 699
[58] Pan R, Fan X L, Zhang H and Yang Y 2016 *Comput. Mater. Sci.* **122** 118
[59] Kang M, Kim B, Ryu S H, Jung S W, Kim J, Moreschini L, Jozwiak C, Rotenberg E, Bostwick A and Kim K S 2017 *Nano Lett.* **17** 1610
[60] Ataca C, Topsakal M, Aktürk E and Ciraci S 2011 *J. Phys. Chem. C* **115** 16354
[61] Zeng H L, Zhu B R, Liu K, Fan J H, Cui X D and Zhang Q M 2012 *Phys. Rev. B* **86** 241301
[62] Luo X, Zhao Y Y, Zhang J, Toh M L, Kloc C, Xiong Q H and Quek S Y 2013 *Phys. Rev. B* **88** 195313
[63] Scheuschner N, Gillen R, Staiger M and Maultzsch J 2015 *Phys. Rev. B* **91** 235409
[64] Yan R s, Simpson J R, Bertolazzi S, Brivio J, Watson M, Wu X f, Kis A, Luo T f, Hight Walker A R and Xing H G 2014 *ACS Nano* **8** 986
[65] Miller B, Parzinger E, Vernickel A, Holleitner A W and Wurstbauer U 2015 *Appl. Phys. Lett.* **106** 122103
[66] Najmaei S, Liu Z, Ajayan P M and Lou J 2012 *Appl. Phys. Lett.* **100** 013106
[67] Peimyoo N, Shang J z, Yang W h, Wang Y l, Cong C x and Yu T 2015 *Nano Res.* **8** 1210
[68] Luo Z, Maassen J, Deng Y, Du Y, Garrelts R P, Lundstrom M S, Ye P D and Xu X 2015 *Nat. Commun.* **6** 8572
[69] Cahangirov S, Sahin H, Le Lay G and Rubio A 2017 *Introduction to the physics of silicene and other 2d materials*, Springer International Publishing, Germany, 1 edn., vol. 930, ch. 6, pp. 87–96
[70] Johari P and Shenoy V B 2012 *ACS Nano* **6** 5449
[71] Krustok J, Raadik T, Jaaniso R, Kiisk V, Sildos I, Marandi M, Komsa H P, Li B, Zhang X, Gong Y and Ajayan P M 2016 *Appl. Phys. Lett.* **109** 253106
[72] Ji J T, Zhang A M, Xia T L, Gao P, Jie Y H, Zhang Q and Zhang Q M 2016 *Chin. Phys. B.* **25** 077802
[73] Ouyang B, Mi Z T and Song J 2016 *J. Phys. Chem. C* **120** 8927
[74] Island J O, Kuc A, Diependaal E H, Bratschitsch R, van der Zant H S, Heine T and Castellanos-Gomez A 2016 *Nanoscale* **8** 2589
[75] Lu N, Guo H, Li L, Dai J, Wang L, Mei W N, Wu X and Zeng X C 2014 *Nanoscale* **6** 2879
[76] Frisenda R, Drüppel M, Schmidt R, Michaelis de Vasconcellos S, Perez de Lara D, Bratschitsch R, Rohlfing M and Castellanos-Gomez A 2017 *npj 2D Materials and Applications* **1**
[77] Yun W S, Han S W, Hong S C, Kim I G and Lee J D 2012 *Phys. Rev. B* **85** 033305
[78] Vasu K, Matte H S S R, Shirodkar S N, Jayaram V, Reddy K P J, Waghmare U V and Rao C N R 2013 *Chem. Phys. Lett.* **582** 105
[79] Hosseini M, Elahi M, Pourfath M and Esseni D 2015 *Appl. Phys. Lett.* **107** 253503
[80] Shen T, Penumatcha A V and Appenzeller J 2016 *ACS Nano* **10** 4712
[81] Huang M, Yan H, Heinz T F and Hone J 2010 *Nano Lett.* **10** 4074
[82] Kim S j and Ryu S m 2016 *Carbon* **100** 283
[83] Rahaman M, Rodriguez R D, Plechinger G, Moras S, Schuller C, Korn T and Zahn D R T 2017 *Nano Lett.* **17** 6027
[84] Desai S B, Seol G, Kang J S, Fang H, Battaglia C, Kapadia R, Ager J W, Guo J and Javey A 2014 *Nano Lett.* **14** 4592
[85] Wang Y, Cong C, Qiu C and Yu T 2013 *Small* **9** 2857
[86] Zhu C R, Wang G, Liu B L, Marie X, Qiao X F, Zhang X, Wu X X, Fan H, Tan P H, Amand T and Urbaszek B 2013 *Phys. Rev. B* **88** 121301
[87] Lloyd D, Liu X, Christopher J W, Cantley L, Wadehra A, Kim B L, Goldberg B B, Swan A K and Bunch J S 2016 *Nano Lett.* **16** 5836
[88] Hui Y Y, Liu X J, Jie W J, Chan N Y, Hao J H, Hsu Y T, Li L J, Guo W L and Lau S P 2013 *ACS Nano* **7** 7126
[89] Buscema M, Steele G A, van der Zant H S J and Castellanos-Gomez A 2014 *Nano Res.* **7** 561
[90] Banszerus L, Janssen H, Otto M, Epping A, Taniguchi T, Watanabe K, Beschoten B, Neumaier D and Stampfer C 2017 *2D Mater.* **4** 025030
[91] Shi J p, Ma D l, Han G F, Zhang Y, Ji Q q, Gao T, Sun J y, Song X j, Li C, Zhang Y s, Lang X y, Zhang Y f and Liu Z f 2014 *ACS Nano* **8** 10196
[92] Sahin H, Tongay S, Horzum S, Fan W, Zhou J, Li J, Wu J and Peeters F M 2013 *Phys. Rev. B* **87** 165409
[93] Zhao W J, Ghorannevis Z, Amara K K, Pang J R, Toh M L, Zhang X, Kloc C, Tan P H and Eda G 2013 *Nanoscale* **5** 9677
[94] Lee C G, Yan H G, Brus L E, Heinz T F, Hone J and Ryu S 2010 *ACS Nano* **4** 2695
[95] Berkdemir A, Gutiérrez H R, Botello-Méndez A R, Perea-López N, Elías A L, Chia C L, Wang B, Crespi V H, López-Urías F and Charlier J C 2013 *Sci. Rep.* **3** 1755
[96] Tan P H, Han W P, Zhao W J, Wu Z H, Chang K, Wang H, Wang Y F, Bonini N, Marzari N and Savini G 2012 *Nat. Mater.* **11** 294
[97] Castellanos Gomez A, Vicarelli L, Prada E, Island J O, Narasimha Acharya K L, Blanter S I, Groenendijk D J, Buscema M, Steele G A and Alvarez J V 2014 *2D Mater.* **1** 025001
[98] Late D J, Liu B, Matte H S S, Rao C N R and Dravid V P 2012 *Adv. Funct. Mater.* **22** 1894
[99] Ferreira E H M, Moutinho M V, Stavale F, Lucchese M M, Capaz R B, Achete C A and Jorio A 2010 *Phys. Rev. B* **82** 125429
[100] Wang H, Yu L, Lee Y H, Shi Y, Hsu A, Chin M L, Li L J, Dubey M, Kong J and Palacios T 2012 *Nano Lett.* **12** 4674
[101] Duan X, Wang C, Shaw J C, Cheng R, Chen Y, Li H, Wu X, Tang Y, Zhang Q, Pan A, Jiang J, Yu R, Huang Y and Duan X 2014 *Nat. Nanotechnol.* **9** 1024
[102] Late D J, Shirodkar S N, Waghmare U V, Dravid V P and Rao C N R 2014 *ChemPhysChem* **15** 1592
[103] Yamamoto M, Wang S T, Ni M Y, Lin Y F, Li S L, Aikawa S, Jian W B, Ueno K, Wakabayashi K and Tsukagoshi K 2014 *ACS Nano* **8** 3895
[104] Chen S Y, Zheng C, Fuhrer M S and Yan J 2015 *Nano Lett.* **15** 2526
[105] Li S l, Miyazaki H s, Son H s, Kuramochi H, Nakaharai S and Tsukagoshi K 2012 *ACS Nano* **6** 7381
[106] Qiao X F, Li X L, Zhang X, Shi W, Wu J B, Chen T and Tan P H 2015 *Appl. Phys. Lett.* **106** 223102
[107] Luo X, Lu X, Cong C, Yu T, Xiong Q and Quek S Y 2015 *Sci Rep.* **5** 14565
[108] Cai Y Q, Lan J H, Zhang G and Zhang Y W 2014 *Phys. Rev. B* **89** 035438
[109] Zhao H, Wu J B, Zhong H X, Guo Q S, Wang X M, Xia F N, Yang L, Tan P H and Wang H 2015 *Nano Res.* **8** 3651
[110] He R, Jeremiah van Baren, Yan J A, Xi X X, Ye Z P, Ye G H, Lu I H, Leong S M and Lui C H 2016 *2D Mater.* **3** 031008
[111] Qiao X F, Wu J B, Zhou L, Qiao J, Shi W, Chen T, Zhang X, Zhang J, Ji W and Tan P H 2016 *Nanoscale* **8** 8324
[112] Das A, Pisana S, Chakraborty B, Piscanec S, Saha S K, Waghmare U V, Novoselov K S, Krishnamurthy H R, Geim A K, Ferrari A C and Sood A K 2008 *Nat. Nanotechnol.* **3** 210
[113] Chakraborty B, Bera A, Muthu D V S, Bhowmick S, Waghmare U V and Sood A K 2012 *Phys. Rev. B* **85** 161403
[114] Xu H J, Wu X M, Li X, Luo C, Liang F, Orignac E, Zhang J and Chu J 2018 *Carbon* **127** 491

[115] Goli P, Khan J, Wickramaratne D, Lake R K and Balandin A A 2012 *Nano Lett.* **12** 5941
[116] Late D J 2015 *ACS Appl. Mat. Interfaces* **7** 5857
[117] Thripuranthaka M and Late D J 2014 *ACS Appl. Mat. Interfaces* **6** 1158
[118] Calizo I, Balandin A A, Bao W, Miao F and Lau C N 2007 *Nano Lett.* **7** 2645
[119] Sahoo S, Gaur A P S, Ahmadi M, Guinel M J F and Katiyar R S 2013 *J. Phys. Chem. C* **117** 9042
[120] Pawbake A S, Island J O, Flores E, Ares J R, Sanchez C, Ferrer I J, Jadkar S R, van der Zant H S, Castellanos-Gomez A and Late D J 2015 *ACS Appl. Mat. Interfaces* **7** 24185
[121] Zhang S, Yang J, Xu R J, Wang F, Li W F, Ghufran M, Zhang Y W, Yu Z F, Zhang G and Qin Q H 2014 *ACS Nano* **8** 9590
[122] Xia J, Li X Z, Huang X, Mao N, Zhu D D, Wang L, Xu H and Meng X M 2016 *Nanoscale* **8** 2063
[123] Chen C C, Li Z, Shi L and Cronin S B 2014 *Nano Res.* **8** 666
[124] Jo I, Hsu I K, Lee Y J, Sadeghi M M, Kim S, Cronin S, Tutuc E, Banerjee S K, Yao Z and Shi L 2011 *Nano Lett.* **11** 85
[125] Novoselov K S, Mishchenko A, Carvalho A and Castro Neto A H 2016 *Science* **353** aac9439
[126] Chen K, Wan X, Xie W, Wen J, Kang Z, Zeng X, Chen H and Xu J 2015 *Adv. Mater.* **27** 6431
[127] Zhang J, Wang J, Chen P, Sun Y, Wu S, Jia Z, Lu X, Yu H, Chen W, Zhu J, Xie G, Yang R, Shi D, Xu X, Xiang J, Liu K and Zhang G 2016 *Adv. Mater.* **28** 1950
[128] Zhang Q, Xiao X, Zhao R, Lv D, Xu G, Lu Z, Sun L, Lin S, Gao X, Zhou J, Jin C, Ding F and Jiao L 2015 *Angew. Chem. Int. Ed.* **54** 8957
[129] Gong Y j, Lei S d, Ye G l, Li B, He Y m, Keyshar K, Zhang X, Wang Q z, Lou J, Liu Z, Vajtai R, Zhou W and Ajayan P M 2015 *Nano Lett.* **15** 6135
[130] He Y M, Yang Y, Zhan Z H and et al. 2016 *Nano Lett.* **16** 3314
[131] Yu J H, Lee H R, Hong S S, Kong D, Lee H W, Wang H, Xiong F, Wang S and Cui Y 2015 *Nano Lett.* **15** 1031
[132] Yu Y F, Hu S, Su L Q, Huang L J, Liu Y, Jin Z H, Purezky A A, Geohegan D B, Kim K W, Zhang Y and Cao L Y 2015 *Nano Lett.* **15** 486
[133] Zhang X Q, Lin C H, Tseng Y W, Huang K H and Lee Y H 2015 *Nano Lett.* **15** 410
[134] Lin Y C, Ghosh R K, Addou R, Lu N, Eichfeld S M, Zhu H, Li M Y, Peng X, Kim M J, Li L J, Wallace R M, Datta S and Robinson J A 2015 *Nat. Commun.* **6** 7311
[135] Mahjouri-Samani M, Lin M W, Wang K, Lupini A R, Lee J, Basile L, Boulesbaa A, Rouleau C M, Puretzky A A, Ivanov I N, Xiao K, Yoon M and Geohegan D B 2015 *Nat. Commun.* **6** 7749
[136] Gong Y, Lin J, Wang X, Shi G, Lei S, Lin Z, Zou X, Ye G, Vajtai R, Yakobson B I, Terrones H, Terrones M, Tay B K, Lou J, Pantelides S T, Liu Z, Zhou W and Ajayan P M 2014 *Nat. Mater.* **13** 1135
[137] Huang C, Wu S, Sanchez A M, Peters J J, Beanland R, Ross J S, Rivera P, Yao W, Cobden D H and Xu X 2014 *Nat. Mater.* **13** 1096
[138] Chen K, Wan X, Wen J, Xie W G, Kang Z W, Zeng X L, Chen H J and Xu J B 2015 *ACS Nano* **9** 9868